

See discussions, stats, and author profiles for this publication at: <https://www.researchgate.net/publication/269999562>

# Photoisomerization of Silyl-Substituted Cyclobutadiene Induced by $\sigma \rightarrow \pi^*$ Excitation: A Computational Study

ARTICLE in THE JOURNAL OF PHYSICAL CHEMISTRY A · DECEMBER 2014

Impact Factor: 2.69 · DOI: 10.1021/jp503220q · Source: PubMed

---

READS

28

## 3 AUTHORS:



Zexing Qu

Nanjing University

7 PUBLICATIONS 67 CITATIONS

[SEE PROFILE](#)



Chen Yang

Nanjing University

1 PUBLICATION 0 CITATIONS

[SEE PROFILE](#)



Chungen Liu

Nanjing University

22 PUBLICATIONS 298 CITATIONS

[SEE PROFILE](#)

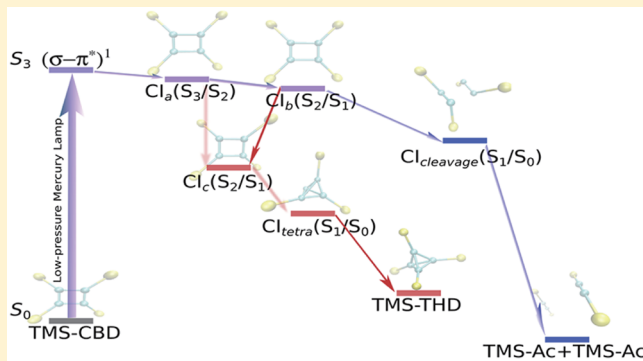
# Photoisomerization of Silyl-Substituted Cyclobutadiene Induced by $\sigma \rightarrow \pi^*$ Excitation: A Computational Study

Zexing Qu, Chen Yang, and Chungen Liu\*

Institute of Theoretical and Computational Chemistry, Key Laboratory of Mesoscopic Chemistry of the Ministry of Education (MOE), School of Chemistry and Chemical Engineering, Nanjing University, Nanjing 210093, China

**S Supporting Information**

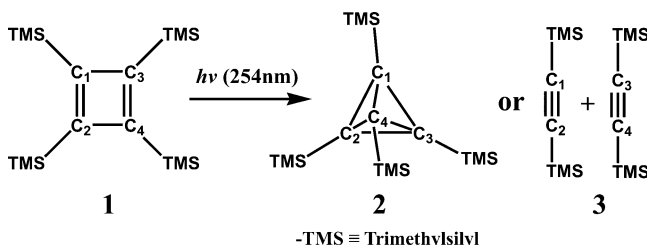
**ABSTRACT:** Photoinduced chemical processes upon Franck–Condon (FC) excitation in tetrakis(trimethylsilyl)-cyclobutadiene (TMS-CBD) have been investigated through the exploration of potential energy surface crossings among several low-lying excited states using the complete active space self-consistent field (CASSCF) method. Vertical excitation energies are also computed with the equation-of-motion coupled-cluster model with single and double excitations (EOM-CCSD) as well as the multireference Møller–Plesset (MRMP) methods. Upon finding an excellent coincidence between the computational results and experimental observations, it is suggested that the Franck–Condon excited state does not correspond to the first  $\pi \rightarrow \pi^*$  single excitation state ( $S_1$ ,  $1^1B_1$  state in terms of  $D_2$  symmetry), but to the second  $1^1B_1$  state ( $S_3$ ), which is characterized as a  $\sigma \rightarrow \pi^*$  single excitation state. Starting from the Franck–Condon region, a series of conical intersections (CIs) are located along one isomerization channel and one dissociation channel. Through the isomerization channel, TMS-CBD is transformed to tetrakis(trimethylsilyl)-tetrahedrane (TMS-THD), and this isomerization process could take place by passing through a “tetra form” conical intersection. On the other hand, the dissociation channel yielding two bis(trimethylsilyl)-acetylene (TMS-Ac) molecules through further stretching of the longer C–C bonds might be more competitive than the isomerization channel after excitation into  $S_3$  state. This mechanistic picture is in good agreement with recently reported experimental observations.



## INTRODUCTION

Ring-strained organic molecules, such as cyclobutadiene (CBD) or tetrahedrane (THD), where the C–C–C bond angles deviate substantially from the ideal  $sp^2$  or  $sp^3$  values, respectively, have generated considerable interest from both experimental and theoretical chemists over the past half century<sup>1–10</sup> because of not only their abnormal bonding properties of general scientific importance but also the possible applications arising from their extraordinary electronic behaviors.<sup>11–13</sup>

Although the unsubstituted CBD and THD molecules are highly unstable, many of their substituted derivatives have been synthesized, showing unexpected thermal stability at or even highly above room temperatures.<sup>14–19</sup> Further studies revealed that interesting photo and thermoisomerizations could take place between CBD and THD frameworks.<sup>17,18,20–23</sup> For instance, tetrakis(trimethylsilyl)-cyclobutadiene (TMS-CBD), which has been successfully synthesized and fully characterized, is a superior photochemical precursor for tetrakis(trimethylsilyl)-tetrahedrane (TMS-THD).<sup>18</sup> Although thermal rearrangement from CBD to THD is symmetry-forbidden, this isomerization process could be initiated by light irradiation.<sup>23,24</sup> Unfortunately, this reaction channel is severely obstructed by a competitive dissociation path yielding two bis(trimethylsilyl)-acetylene (TMS-Ac) molecules, as shown in Scheme 1. So far, the only

**Scheme 1**

reported successful synthesis was implemented at an extremely low temperature of  $-130\text{ }^\circ\text{C}$ , upon a sustained very long time irradiation using a low-pressure mercury lamp (254 nm).<sup>18</sup>

Theoretically, irradiation-initiated conversion from CBD to THD has also been studied recently, which followed the  $S_1 \rightarrow S_0$  transition path through a tetra-radical form conical intersection ( $\text{Cl}_{\text{tetra}}$ ).<sup>24–26</sup> Franck–Condon (FC) excitation was assigned to the  $S_1$  state, which is attributed to  $1^1B_1$  state (in terms of  $D_2$  symmetry), corresponding to a  $\pi \rightarrow \pi^*$  single excitation.

**Received:** December 20, 2013**Revised:** December 22, 2014**Published:** December 23, 2014

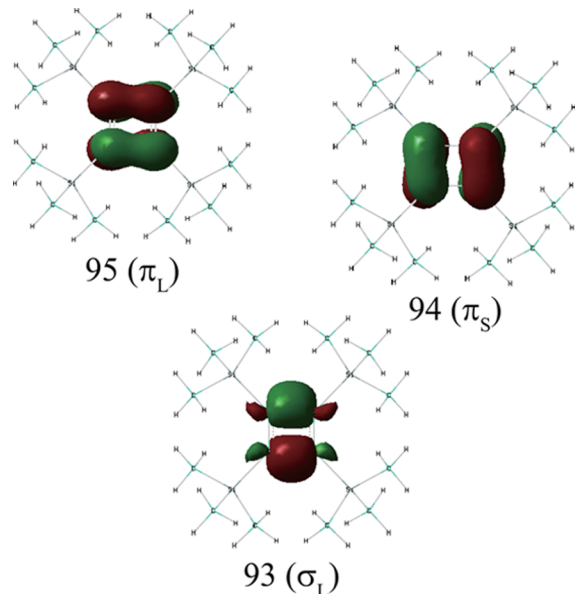


**Figure 1.** Illustration of the three most active natural orbitals involved in the description of the low-lying excited states, which are computed with the ground state geometry. The subscripts “S” and “L” indicate the natural orbitals located on shorter and longer C–C bonds, respectively. The major electronic configurations as well as oscillator strengths (*f*) are computed at the CASSCF(12,12)/6-31G(d) level.

However, near  $\text{Cl}_{\text{tetra}}$  point,  $S_1$  is characterized as a  $\pi \rightarrow \pi^*$  double excitation state ( $2^1\text{A}$  state at FC point), which implies that there should exist a crossing between  $1^1\text{B}_1$  and  $2^1\text{A}$  states located between FC and  $\text{Cl}_{\text{tetra}}$  points on the  $S_1$  potential energy surface (PES). The electronic structure changes at  $\text{Cl}_{\text{tetra}}$  could be reasonably explained by this mechanism, because it has been well documented that the  $\pi \rightarrow \pi^*$  double excitation configuration in the  $S_1$  state of CBD becomes the major component in the ground state electronic wave function of THD.<sup>23–25,27</sup> However, there are at least two questions yet to be answered. First, experimentally, two absorptions had been observed for CBD derivatives, with one strong absorption centered at ca. 300 nm and a weak band at >400 nm. Although both of them were assigned to optically allowed  $1^1\text{B}_1$  states,<sup>14,18,19</sup> the electronic character of both states has not been well elucidated. Second, this mechanism did not explain the easily observed dissociation channel. Actually,  $\pi \rightarrow \pi^*$  single excitation could only weaken the  $\pi$  bonds, whereas C–C bond cleavage is expected to take place upon  $\sigma$  bond excitation.

To answer these questions, it is necessary to recompute the vertical excitation energies using high-level ab initio methods, which include adequate description of both nondynamical and dynamical correlations. On the other hand, the  $\sigma \rightarrow \pi^*$  characterized  $S_3$  state ( $2^1\text{B}_1$  state at FC point) should be included in addition to  $S_1$  and  $S_2$  states in order to understand the dissociation path. For TMS-CBD, our calculations will show that the most intensive absorption near 300 nm should be assigned to  $S_3$  state rather than  $S_1$  state. On the basis of the  $S_0 \rightarrow S_3$  FC excitation, we would suggest an alternative mechanism which could provide a consistent explanation on both reaction channels. Information about the geometrical and electronic properties of the critical points including minimum points and conical intersections on relevant potential energy surfaces will be presented with detailed analyses. Relations among these stationary points will be discussed with emphases on their importance in helping us understand the experimental findings.<sup>18,28</sup>

State	Configuration	<i>f</i>
$S_0$ (GS)	82.4% (94) <sup>2</sup> (95) <sup>0</sup>	-
$S_1$	86.1% (94) <sup>1</sup> (95) <sup>1</sup>	0.00056
$S_2$	76.0% (94) <sup>0</sup> (95) <sup>2</sup>	-
$S_3$	81.8% (93) <sup>1</sup> (95) <sup>1</sup>	0.00154

## COMPUTATIONAL DETAILS

Because the  $D_2$  group symmetry is maintained in all the minimum point geometries of relevant states, we use its irreducible representation labels  $A$  and  $B_1$  to indicate the symmetry of the electronic states. However, along the reaction coordinates, in-plane and out-of-plane distortions can break the  $D_2$  symmetry. Accordingly, we use the adiabatic state labels ( $S_n$ ) when referring to state transitions.

Potential energy surface crossings among several lower-lying excited states as well as the ground state are calculated at the level of complete active space self-consistent field (CASSCF),<sup>29,30</sup> spanned with 12 electrons distributed in four  $\pi$  orbitals and eight  $\sigma$  orbitals on the CBD core, which ensures a reliable computation of the nondynamical electron correlation both in the CBD to THD isomerization process and in the dissociation process of the CBD core. The critical points on the potential energy surfaces, including equilibrium geometries of the ground and excited states are optimized with the state-averaged CASSCF method. The minimum energy conical intersection (MECI, hereafter abbreviated as “conical intersection”) points are optimized following Robb’s strategy.<sup>31</sup> To investigate the effect of dynamic correlation on excitation energies, single-point calculations are also performed with the equation-of-motion coupled-cluster model with single and double excitations (EOM-CCSD)<sup>32</sup> as well as the Multi-Reference Møller–Plesset (MRMP)<sup>33,34</sup> methods for some characteristic geometries on the potential energy surfaces. MRMP calculations are performed on the reference function obtained with a state-averaged CASSCF-(12,12) calculation including four lowest singlet states. Although the EOM-CCSD method is a highly recommended method for computing excitation energies within the single reference framework, the computational error is found to be quite too large for the doubly excited  $S_2$  state of CBD. For systems like CBD, whose target states are multiconfigurational due to orbital degeneracies, the reference state should be chosen as a high-spin state, and the low-spin state could be obtained by the spin-flip EOM operators (EOM-SF models).<sup>35</sup> Furthermore, for a better description of the double-excitation character in the  $S_2$  state of

CBD, one needs to expand the configuration interaction basis set for the similarity-transformed Hamiltonian; however, it is presently too time-consuming and storage-demanding for systems as large as TMS-CBD.

Implementation of the mixed basis (MixB) set has been shown to be very effective in cutting down the computational cost without serious loss of accuracy in computing CBD derivatives with tetra-*tert*-butyl substituents.<sup>26</sup> In this work, this strategy is employed by combining the 6-31G(d) basis set<sup>36–40</sup> (for the atoms on the CBD core) and STO-3G basis set<sup>41,42</sup> (for the atoms on the substituents). However, the full 6-31G(d) basis set is employed in computing the ground state geometry as well as the vertical excitation energies.

Density functional theory (DFT) calculations using the B3LYP functional<sup>43–46</sup> are performed using GAUSSIAN package.<sup>47</sup> Although the MOLPRO package is used for CASSCF and EOM-CCSD calculations,<sup>48</sup> GAMESS package is for MRMP calculations.<sup>49,50</sup>

## RESULTS AND DISCUSSION

**Franck–Condon Excitation.** To elucidate the mechanism of the photochemical process starting from TMS-CBD, we begin with the study of the Franck–Condon excitation. The geometry optimization at the level of B3LYP/6-31G(d) indicates a ground state structure of  $D_2$  symmetry, in which the CBD core is slightly distorted from the planar conformation.

Because the following multireference calculations are performed with natural orbitals obtained from a preceding CASSCF calculation, detailed analysis of the natural orbitals that are involved deeply in FC excitation, as well as in succeeding reaction steps, is helpful in understanding the evolution of electronic wave function along each reaction channel. In Figure 1, we illustrate two  $\pi$ -type natural orbitals 94 ( $\pi_S$ ) and 95 ( $\pi_L$ ), and one  $\sigma$ -type natural orbital 93 ( $\sigma_L$ ). Obviously, orbitals 94 and 95 have a nodal plane perpendicular to the CBD moiety, bisecting the two longer or shorter bonds, respectively, similar to the Hartree–Fock HOMO or LUMO molecular orbitals. Orbital 93 is located on the two longer bonds, which indicates that it could be easily excited. It is worth noticing that all of these frontier orbitals are essentially composed of the atomic orbitals in the CBD core, which implies that the bulky substituents should mostly affect the FC excitations through the dynamical correlation instead of the static correlation.

On the basis of these orbitals, the three lowest excited states are analyzed, with the major components in the wave functions as well as the oscillator strengths collected in Figure 1. In sequence of excitation energy,  $S_1$  is the first optically allowed excited state of  $B_1$  symmetry, characterized as  $\pi_S \rightarrow \pi_L$  single excitation, with a small oscillator strength;  $S_2$  ( $2^1A$ ) is the first optically forbidden state with predominant  $\pi_S^2 \rightarrow \pi_L^2$  double-electron excitation. The excitation characters of  $S_1$  and  $S_2$  are similar to those of unsubstituted CBD, which were calculated with EOM-SF-CCSD and multireference average-quadratic coupled cluster (MR-AQCC) methods.<sup>35,51</sup> Above them,  $S_3$  ( $2^1B_1$ ) is again optically allowed with a much larger oscillator strength than  $S_1$  and is dominated by  $\sigma_L \rightarrow \pi_L$  single excitation.

To evaluate the effect of the dynamical electronic correlation, against the CASSCF results, we list in Table 1 the vertical excitation energies computed with several high-level ab initio methods including EOM-CCSD and MRMP, which are expected to agree better with the experimental observations. It could be seen that CASSCF results compare well with MRMP ones in predicting the excitation energy of  $S_2$  state; the disagreements

**Table 1. Vertical Excitation Energies of the Three Lowest Excited States at the Ground State Equilibrium Geometry<sup>a</sup>**

method	$\Delta E_{S_1-GS}$ (eV)	$\Delta E_{S_2-GS}$ (eV)	$\Delta E_{S_3-GS}$ (eV)
CASSCF(12,12)/MixB	3.64	3.99	5.22
CASSCF(12,12)/6-31G(d)	3.48	3.76	5.02
MRMP(12,12)/MixB	3.07	3.80	4.31
EOM-CCSD/MixB	3.13	-	4.10
EOM-CCSD/6-31G(d)	2.95	-	3.99
exptl	2.74 <sup>b</sup> (2.68) <sup>c</sup>	-	3.44 <sup>b,d</sup> (3.98) <sup>c</sup>

<sup>a</sup>Ground-state equilibrium geometry is optimized with B3LYP/6-31G(d) method. <sup>b</sup>Obtained from UV-vis spectroscopy of TMS-CBD in hexane.<sup>18</sup> <sup>c</sup>From UV-vis spectroscopy of perfluoroaryl tetrahedrane in hexane.<sup>19</sup> <sup>d</sup>This was originally reported as 226 nm (5.49 eV) in ref 18 and has been corrected with confirmation from the author through a private communication.

among CASSCF, MRMP, and EOM-CCSD results are around 0.5 eV for  $S_1$  state; however, for the  $S_3$  state, the excitation energy is more than 1 eV overestimated by CASSCF in comparison with the results from MRMP and EOM-CCSD calculations. It is not difficult to understand the unbalanced accuracy of CASSCF method in computing different electronic states. With all  $\pi$  and  $\sigma$  electrons in the CBD core included in the active space, the  $\sigma$ - $\pi$  polarization effect can be addressed satisfactorily in computing both  $S_1$  and  $S_2$  states, which are characterized as  $\pi \rightarrow \pi^*$  excitations. On the other hand, the  $S_3$  state corresponds to the  $\sigma \rightarrow \pi^*$  excitation, where dynamical electronic correlation between the CBD core and the attached bulky groups should be included. Hence, for a reliable prediction of the excitation energies for different electronic states of TMS-CBD, a balanced treatment of  $\sigma$ - $\pi$  as well as  $\pi$ - $\pi$  electronic interactions is necessary. Similar to the previous study of unsubstituted CBD, the EOM-CCSD method could still present qualitatively correct excitation energies for singly excited  $S_1$  and  $S_3$  states, even though the ground state of TMS-CBD is substantially multiconfigurational.<sup>35</sup>

We note that the EOM-CCSD method predicts the vertical excitation energies to be around 3.99 eV (~310 nm) and 2.95 eV (~420 nm) for  $S_3$  and  $S_1$  states, respectively. Since the  $S_3$  state is located above the  $S_1$  state and presents a much greater oscillator strength, we could reasonably assign the  $S_3$  state to the stronger absorption peak experimentally observed at 311 nm,<sup>18</sup> while  $S_1$  state to the much weaker band around 462 nm, in contrast with the study of tetra-*tert*-butyl substituted CBD, where the main absorption at approximately 300 nm is assigned to  $S_1$  state.<sup>24,25</sup> Considering the experimental findings where a UV irradiation with low-pressure mercury lamp (254 nm) is applied,<sup>18</sup> the photoinduced isomerization process of TMS-CBD could be initiated from both  $S_1$  and  $S_3$  states.

In the next section, we will show that upon the  $S_0 \rightarrow S_3$  excitation, in addition to the isomerization channel connected to TMS-THD, the dissociation channel could also be opened after passing through one  $S_3/S_2$  conical intersection.

**Mechanism for Photoreactions.** Locating various critical points on relevant potential energy surfaces could be very helpful in understanding the mechanism of photochemical reactions. These critical points include the minimum points on the PES of relevant states, as well as the conical intersections between PES's along possible reaction paths. In this section, characteristic geometrical parameters of minimum points are tabulated in Table 2, and those of CI points can be found in Figures 2, 4, and

**Table 2. Characteristic Geometrical Parameters of the Minimum Points on Low-Lying Electronic States for TMS-CBD, Which Are Calculated with the CASSCF(12,12)/MixB Method**

	(1 <sup>1</sup> A) <sub>min</sub> (S <sub>0</sub> )	(2 <sup>1</sup> A) <sub>min</sub> (S <sub>1</sub> )	(1 <sup>1</sup> B <sub>1</sub> ) <sub>min</sub> (S <sub>2</sub> )	(2 <sup>1</sup> B <sub>1</sub> ) <sub>min</sub> (S <sub>3</sub> )
bond length (Å)				
C <sub>1</sub> —C <sub>3</sub>	1.621	1.490	1.475	1.674
C <sub>1</sub> —C <sub>2</sub>	1.387	1.490	1.475	1.376
C <sub>1</sub> —Si	1.918	1.912	1.911	1.911
dihedral angle (deg)				
C <sub>1</sub> C <sub>2</sub> C <sub>4</sub> C <sub>3</sub>	4.8	5.1	5.5	1.3

5. The relative energies as well as the electronic characters of relevant states are presented in Scheme 2, Tables 3, 4, and Figure

**Table 3. Major Components in the Electronic Wavefunctions of Low-Lying Excited States at the Equilibrium Geometries (D<sub>2</sub> Symmetry) Obtained at CASSCF(12,12)/MixB Level**

	(S <sub>0</sub> ) <sub>min</sub>	(S <sub>1</sub> ) <sub>min</sub>	(S <sub>2</sub> ) <sub>min</sub>	(S <sub>3</sub> ) <sub>min</sub>
1 <sup>1</sup> A	(π <sub>S</sub> ) <sup>2</sup> (π <sub>L</sub> ) <sup>0</sup>	(π <sub>S</sub> ) <sup>2</sup> (π <sub>L</sub> ) <sup>0</sup>	(π <sub>S</sub> ) <sup>2</sup> (π <sub>L</sub> ) <sup>0</sup>	(π <sub>S</sub> ) <sup>2</sup> (π <sub>L</sub> ) <sup>0</sup>
	82.4%	44.0%	44.3%	83.7%
		(π <sub>S</sub> ) <sup>0</sup> (π <sub>L</sub> ) <sup>2</sup>	(π <sub>S</sub> ) <sup>0</sup> (π <sub>L</sub> ) <sup>2</sup>	
2 <sup>1</sup> A		44.0%	44.2%	
	(π <sub>S</sub> ) <sup>0</sup> (π <sub>L</sub> ) <sup>2</sup>	(π <sub>S</sub> ) <sup>2</sup> (π <sub>L</sub> ) <sup>0</sup>	(π <sub>S</sub> ) <sup>2</sup> (π <sub>L</sub> ) <sup>0</sup>	(π <sub>S</sub> ) <sup>0</sup> (π <sub>L</sub> ) <sup>2</sup>
	76.0%	41.4%	41.8%	75.0%
1 <sup>1</sup> B <sub>1</sub>		(π <sub>S</sub> ) <sup>0</sup> (π <sub>L</sub> ) <sup>2</sup>	(π <sub>S</sub> ) <sup>0</sup> (π <sub>L</sub> ) <sup>2</sup>	
		41.4%	41.8%	
	(π <sub>S</sub> ) <sup>1</sup> (π <sub>L</sub> ) <sup>1</sup>	(π <sub>S</sub> ) <sup>1</sup> (π <sub>L</sub> ) <sup>1</sup>	(π <sub>S</sub> ) <sup>1</sup> (π <sub>L</sub> ) <sup>1</sup>	(π <sub>S</sub> ) <sup>1</sup> (π <sub>L</sub> ) <sup>1</sup>
2 <sup>1</sup> B <sub>1</sub>	86.1%	90.2%	90.6%	83.3%
	(σ <sub>L</sub> ) <sup>1</sup> (π <sub>L</sub> ) <sup>1</sup>	(σ <sub>L</sub> ) <sup>1</sup> (π <sub>L</sub> ) <sup>1</sup>	(σ <sub>L</sub> ) <sup>1</sup> (π <sub>L</sub> ) <sup>1</sup>	(σ <sub>L</sub> ) <sup>1</sup> (π <sub>L</sub> ) <sup>1</sup>
	81.8%	43.1%	43.5%	80.8%
(σ <sub>S</sub> ) <sup>1</sup> (π <sub>S</sub> ) <sup>1</sup>		(σ <sub>S</sub> ) <sup>1</sup> (π <sub>S</sub> ) <sup>1</sup>		
		43.1%	43.4%	

6. Cartesian coordinates, absolute energies, and major components of electronic configuration of all adiabatic states at all geometries are provided in the Supporting Information.

**Minimum Points.** As expected, the CBD skeleton of TMS-CBD presents alternating C—C bond lengths due to a pseudo-Jahn–Teller effect, which is similar to an unsubstituted CBD molecule.<sup>4,52,53</sup> Meanwhile, the electron-donating silyl groups increase the occupancy of the antibonding orbitals of the CBD core, which will further stretch the two longer C—C bonds by approximately 0.12 Å compared with the unsubstituted CBD.<sup>52</sup> Such a kind of bond length elongation can cancel out a large portion of the σ<sub>L</sub> → π<sub>L</sub> excitation energy by raising up the energy of σ<sub>L</sub> orbital.

The geometrical character of S<sub>1</sub> state differs from that of S<sub>0</sub> state mainly in the equalized bond lengths on the CBD ring valued at 1.49 Å. This higher geometrical symmetry for the S<sub>1</sub>

state could also be understood in view of the vibronic coupling between S<sub>0</sub> and S<sub>1</sub> states through a rectangular distortion mode, which could stabilize the S<sub>0</sub> state while destabilizing the S<sub>1</sub> state.<sup>4,52,54</sup> Accordingly, the CBD core distorts in a rectangular way in S<sub>0</sub> state, while maintaining its square geometry in the S<sub>1</sub> state. The electronic wave function of the S<sub>1</sub> state at its equilibrium geometry is characterized as the symmetrical combination of two degenerate configurations, (π<sub>S</sub>)<sup>0</sup>(π<sub>L</sub>)<sup>2</sup> and (π<sub>S</sub>)<sup>2</sup>(π<sub>L</sub>)<sup>0</sup>, presenting A symmetry, as shown in Table 3. These two configurations are degenerate because the energy gap disappears between orbitals π<sub>L</sub> and π<sub>S</sub> due to the bond length equalization. At this geometry, the wave function of S<sub>0</sub> state is essentially an antisymmetrical combination of the above two configurations. The intensive mixing of the two configurations opens a gap between the two electronic states, which could subside on twisting the planar CBD ring to the pyramidal conformation, leading to a CI point between the S<sub>1</sub> and S<sub>0</sub> states.<sup>24</sup> Speaking of point group symmetry, the S<sub>1</sub> state at its own equilibrium geometry is correlated with the S<sub>2</sub> state at the ground-state equilibrium geometry.

At the minimum point of the S<sub>2</sub> PES, the bond lengths on the CBD ring are also equalized. The electronic wave function of this state is in B<sub>1</sub> symmetry, characterized as the (π<sub>S</sub>)<sup>1</sup>(π<sub>L</sub>)<sup>1</sup> single excitation. It is obviously correlated with the S<sub>1</sub> state at the ground state equilibrium geometry, which implies that an S<sub>1</sub>/S<sub>2</sub> conical intersection could be located at somewhere between the S<sub>0</sub> and S<sub>2</sub> (or S<sub>1</sub>) PES minimum points. Further analysis of this crossing point will be presented later.

The electronic wave function of the S<sub>3</sub> state at its equilibrium geometry is in B<sub>1</sub> symmetry, attributed to the σ<sub>L</sub> → π<sub>L</sub> single excitation, which is unchanged with respect to the wave function at the FC region (see Table 3). By comparing the equilibrium geometries in S<sub>0</sub> and S<sub>3</sub> states, it could be found that the two longer bonds in the CBD core are stretched by approximately 0.05 Å, whereas the shorter bonds are slightly contracted by 0.01 Å in S<sub>3</sub> state. This point is particularly important because of its relevance to the dissociation process. By stretching the two longer C—C bonds, σ<sub>L</sub> orbital energy is raised up to the frontier position, which manifests its essential role in the internal transition processes initiated from the S<sub>3</sub> state.

**S<sub>3</sub>/S<sub>2</sub> Conical Intersection.** As shown in Figure 2 and Scheme 2, the S<sub>3</sub>/S<sub>2</sub> CI point is labeled as CI<sub>a</sub>. Starting from the FC point on the S<sub>3</sub> PES, going downhill to the minimum point, the CBD skeleton maintains its near-planar conformation, while the two longer C—C bonds are considerably stretched, and the two short ones slightly contracted. The CI<sub>a</sub> point could be found at somewhere very close to the energy minimum on the S<sub>3</sub> PES, with less than 0.001 Å bond length deviations between these two structures. It is expected that an approach to this CI point should be straightforward upon an excitation to the S<sub>3</sub> PES.

The probability of an internal conversion through a CI point could be calculated as the scalar product of “derivative coupling

**Table 4. Contribution of Major Electronic Configurations in Relevant States at Three Conical Intersections Calculated at CASSCF(12,12)/MixB Level**

CI <sub>a</sub>	S <sub>3</sub>	S <sub>2</sub>	S <sub>2</sub>	CI <sub>b</sub>	S <sub>1</sub>	S <sub>2</sub>	S <sub>1</sub>	CI <sub>c</sub>
(σ <sub>L</sub> ) <sup>1</sup> (π <sub>L</sub> ) <sup>1</sup>		(σ <sub>L</sub> ) <sup>1</sup> (π <sub>L</sub> ) <sup>1</sup>	(σ <sub>L</sub> ) <sup>1</sup> (π <sub>L</sub> ) <sup>1</sup>		(σ <sub>L</sub> ) <sup>1</sup> (π <sub>L</sub> ) <sup>1</sup>		(σ <sub>S</sub> ) <sup>0</sup> (π <sub>L</sub> ) <sup>2</sup>	
84.6%		<1.0%	53.8%		31.8%	73.4%	3.3%	
(π <sub>S</sub> ) <sup>0</sup> (π <sub>L</sub> ) <sup>2</sup>		(π <sub>S</sub> ) <sup>0</sup> (π <sub>L</sub> ) <sup>2</sup>	(π <sub>S</sub> ) <sup>1</sup> (π <sub>L</sub> ) <sup>1</sup>		(π <sub>S</sub> ) <sup>1</sup> (π <sub>L</sub> ) <sup>1</sup>	(π <sub>S</sub> ) <sup>1</sup> (π <sub>L</sub> ) <sup>1</sup>	(π <sub>S</sub> ) <sup>1</sup> (π <sub>L</sub> ) <sup>1</sup>	
<1.0%		75.5%	31.1%		52.9%	2.8%	86.9%	

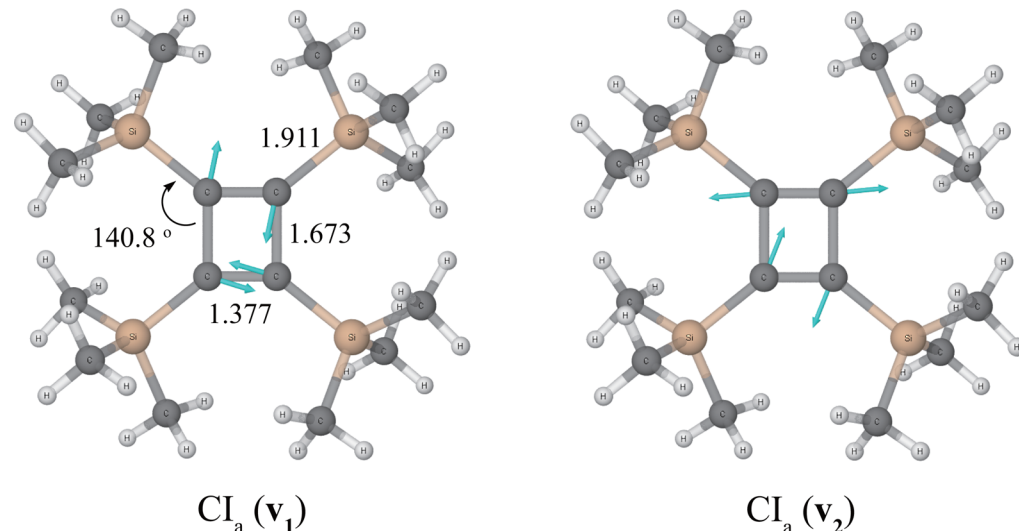
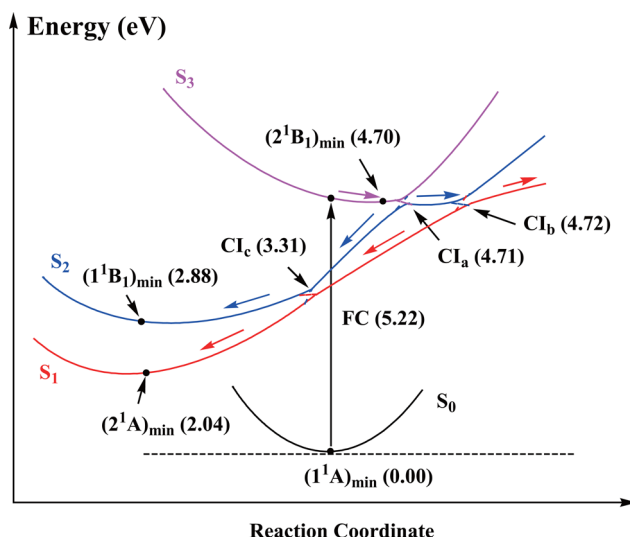


**Figure 2.** Geometry of TMS-CBD at  $S_3/S_2$  conical intersection ( $CI_a$ ) optimized at CASSCF(12,12)/MixB level, with the illustration of the derivative coupling vector  $v_1$  and the gradient difference vector  $v_2$ .

**Scheme 2. Schematic Energy Profile of the Potential Energy Surfaces of Four Low-Lying States along the Relaxation Coordinate<sup>a</sup>**



<sup>a</sup>The energies of critical points relative to the ground state energy are presented in brackets. The arrows indicate the possible relaxation paths via these CI points.

vector" of the two relevant electronic states and the velocity of nuclei<sup>55</sup>

$$d_{12} = \langle \psi_1 | \frac{\partial}{\partial \mathbf{R}} \psi_2 \rangle \cdot \mathbf{v} \quad (1)$$

where  $\mathbf{v} \equiv d\mathbf{R}/dt$  refers to the velocity of the nuclei, while the first term is the derivative coupling vector, which indicates the strength of the non-adiabatic coupling of the two crossing states. Although the derivative coupling vector of a CI point can be computed with the electronic wavefunctions of the two crossing states, the information on nuclear dynamics is only available from non-adiabatic dynamics simulations. Considering the vibronic coupling effect, the non-adiabatic transition could follow any directions in the branching plane of the CI point,<sup>31,56</sup> depending jointly on the directions of both the derivative coupling vector

and the nuclear velocity at the moment of state transition. Consequently, after passing through this CI point, two relaxation channels connecting to  $CI_b$  and  $CI_\sigma$ , respectively, will be opened, as shown in Scheme 2. The efficiency of the two channels can be evaluated through a statistical analysis of an ensemble of relaxation trajectories obtained from non-adiabatic dynamics simulations.

As has been discussed earlier, the dynamical correlation plays a critical role in the description of the  $S_3$  state, for this reason we calculated the energy profile of relevant states along the interpolated path from the FC region to  $CI_a$  with both CASSCF and MRMP methods. As shown in Figure 3, it could be found that the two potential energy surfaces at MRMP level may intersect at a lower energy region than is predicted with CASSCF method, this is due to the fact that the substituent effect, which plays a non-negligible role in further stabilizing the  $S_3$  state, is accounted for as the dynamical correlation energy in MRMP treatment, while it is ignored in CASSCF calculations.

At a conical intersection, two vibrational modes can be defined, which will lift the degeneracy of the two states.<sup>31</sup> One is the previously mentioned derivative coupling vector  $v_1 = \langle \psi_i | (\partial/\partial \mathbf{R}) \psi_j \rangle$ ; the other is the gradient difference vector  $v_2 = \partial(E_i - E_j)/\partial \mathbf{R}$ , where  $E_i$  and  $E_j$  are the upper and lower state energies, respectively. In Figure 2, we also present derivative coupling vector as well as the gradient difference vector at  $CI_a$ . Note that the combination of the two vectors at  $CI_a$  point could generate two relaxation directions leading to either the dissociation of the CBD skeleton or the isomerization of it to THD structure.

**$S_2/S_1$  Conical Intersections.** Between the  $S_2$  and  $S_1$  potential energy surfaces, two CI points are located, which are labeled as  $CI_b$  and  $CI_\sigma$ , respectively, as shown in Figure 4. Let us take a look at one of the two crossing points,  $CI_b$ . After passing through the  $CI_a$  point, along with the further stretching of the two longer C-C bonds, the  $S_2$  state retains its major configuration of  $\sigma_L \rightarrow \pi_L$  single excitation, which was inherited from the original  $S_3$  state, whereas the  $S_1$  state keeps its major configuration of  $\pi_S \rightarrow \pi_L$  single excitation (see Table 4). Accordingly, the adiabatic wave functions of the two degenerate states at  $CI_b$  should be constructed with these two major configurations, as shown in Table 4. In a specific nonadiabatic dynamics trajectory, the way of mixing of the two configurations is determined by the vibronic

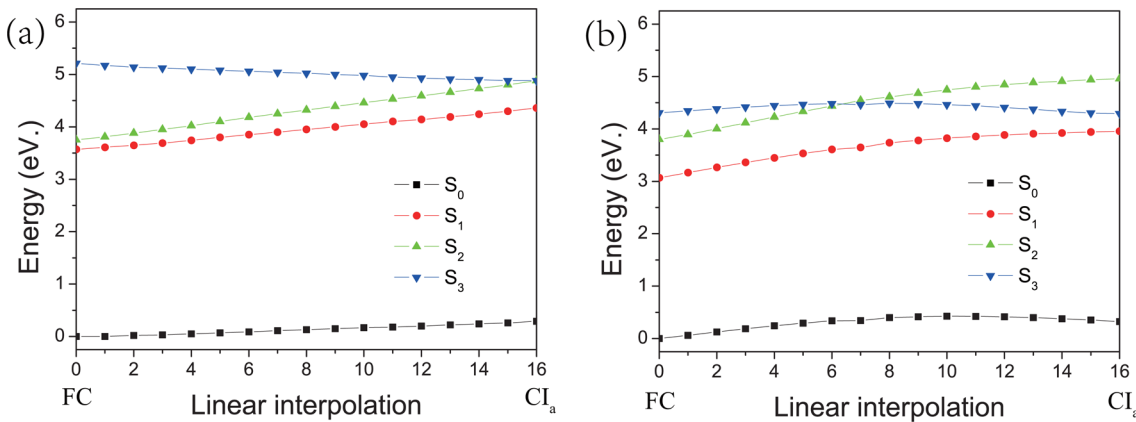


**Figure 3.** Energy profile of the relaxation path of  $S_3$  state from the FC region to the  $S_3/S_2$  conical intersection ( $CI_a$ ): calculated at (a) CASSCF(12,12)/MixB level, (b) MRMP(12,12)/MixB level. The molecular geometries are derived by linear interpolations between FC and  $CI_a$  geometries calculated with CASSCF(12,12)/MixB method.

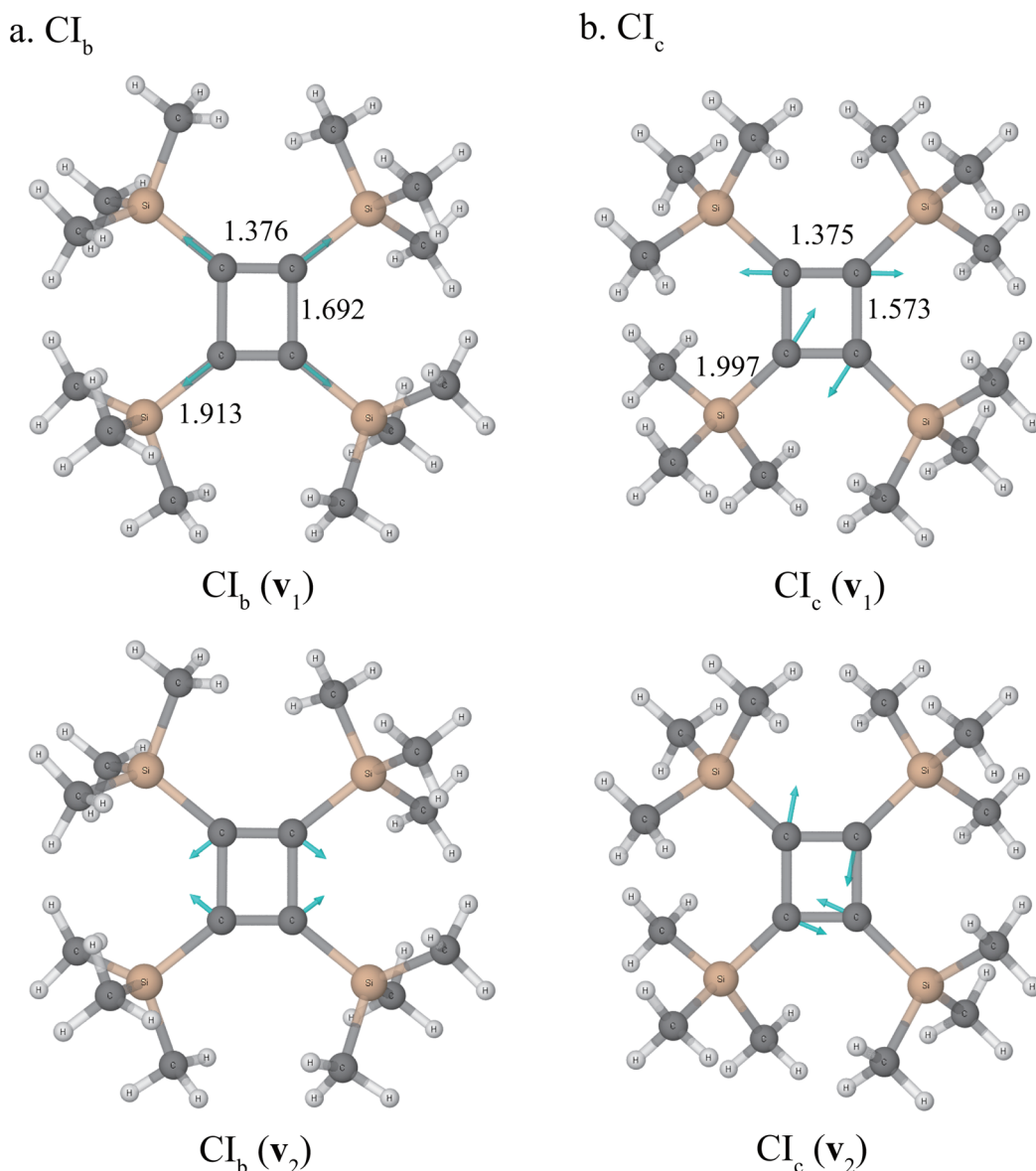


**Figure 4.** Geometries of TMS-CBD at  $S_2/S_1$  CI points, (a)  $CI_b$ ; (b)  $CI_c$ , optimized at CASSCF(12,12)/MixB level. The derivative coupling vector  $v_1$  and the gradient difference vector  $v_2$  are shown as well.

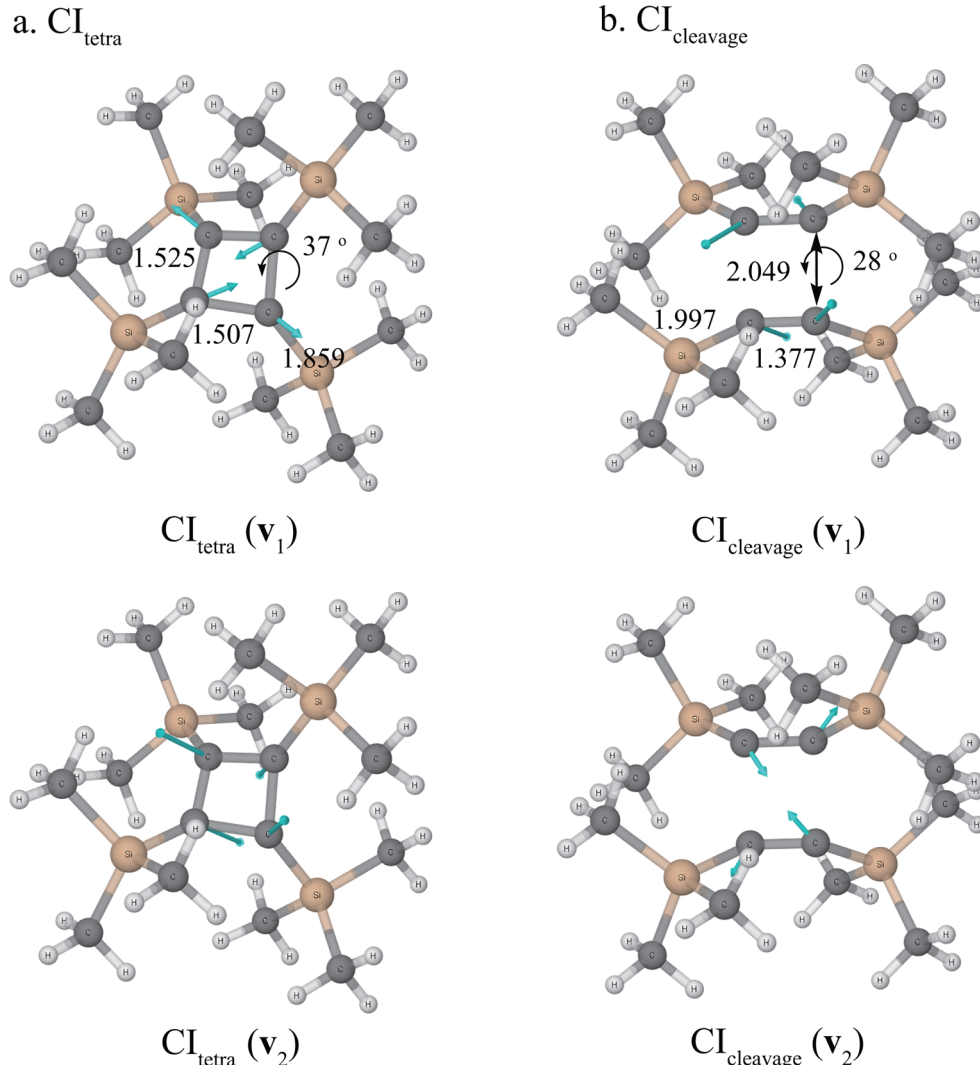


**Figure 5.** Geometries of TMS-CBD at  $S_1/S_0$  conical intersections, (a)  $\text{CI}_{\text{tetra}}$ ; (b)  $\text{CI}_{\text{cleavage}}$ , optimized at CASSCF(12,12)/MixB level, as well as the derivative coupling vector  $\mathbf{v}_1$  and the gradient difference vector  $\mathbf{v}_2$ .

coupling between the two relevant states, which opens two possible relaxation paths linking to the  $\text{CI}_c$  and the  $\text{CI}_{\text{cleavage}}$  (which will be discussed later), respectively. The way of geometrical transformation in the two relaxation paths after passing through  $\text{CI}_b$  could be rationalized by exploring the two vectors  $\text{CI}_b (\mathbf{v}_1)$  and  $\text{CI}_b (\mathbf{v}_2)$ . The sum of them defines a C–C bond breaking channel connected to two dissociated TMS-Ac molecules, whereas their difference defines a channel to  $\text{CI}_c$ , where the two longer C–C bonds in CBD skeleton are shortened.

$\text{CI}_c$  is another crossing point between the  $S_2$  and  $S_1$  potential energy surfaces, which is located beneath the  $\text{CI}_b$ . In principle, this CI point could be reached from both  $\text{CI}_a$  and  $\text{CI}_b$  via downhill relaxation pathways. Following these pathways, the longer C–C bond is considerably contracted by approximately 0.1 Å, resulting in significant stabilization of  $\sigma_L$  orbital. When arriving at the  $\text{CI}_c$  point, the adiabatic wave functions of the two near-degenerate states  $S_2$  and  $S_1$  is composed of two characteristic configurations,  $\pi_S \rightarrow \pi_L$  double excitation and  $\pi_S \rightarrow \pi_L$  single excitation, which are inherited from the  $S_2$  and  $S_1$  states at the FC region, respectively, as shown in Table 4. Around this CI point, considering the vibronic coupling effect,<sup>57,58</sup> two relaxation paths should be opened, one to the  $S_2$  minimum, the other to  $\text{CI}_{\text{tetra}}$  (a

$S_1/S_0$  crossing point, which will be discussed shortly later). This could be helpful in understanding the 50% yield of conversion from TMS-CBD to TMS-THD upon a 70 h irradiation.<sup>18</sup> If the system moves on the  $S_2$  PES toward the  $S_2$  minimum point, the molecule could undergo transition to the ground state either through vibronic relaxation, whereas if it moves on  $S_1$  PES, the isomerization process could be fulfilled by passing through  $\text{CI}_{\text{tetra}}$ . We note that similar isomerization processes were studied previously in CBD as well as its tetra-*tert*-butyl-substituted derivatives.<sup>24–26</sup>

A schematic energy profile of relevant electronic states along the relaxation paths is presented in Scheme 2, which is used to illustrate the relationship among the above-discussed critical points. It could be seen that, after FC excitation to  $S_3$  state, the system follows a downhill path and quickly approaches the  $S_3/S_2$  conical intersection point ( $\text{CI}_a$ ), two decaying channels are followed afterward, linked to  $\text{CI}_c$  by contracting the longer C–C bonds, and  $\text{CI}_b$  through further stretching of the longer C–C bonds. Later, by passing through  $\text{CI}_b$ , two relaxation channels are opened toward either the dissociation of the CBD skeleton or the other  $S_2/S_1$  conical intersection ( $\text{CI}_c$ ). After  $\text{CI}_c$ , two relaxation paths leading to the  $S_2$  minimum point and  $\text{CI}_{\text{tetra}}$ , respectively, are also proposed.

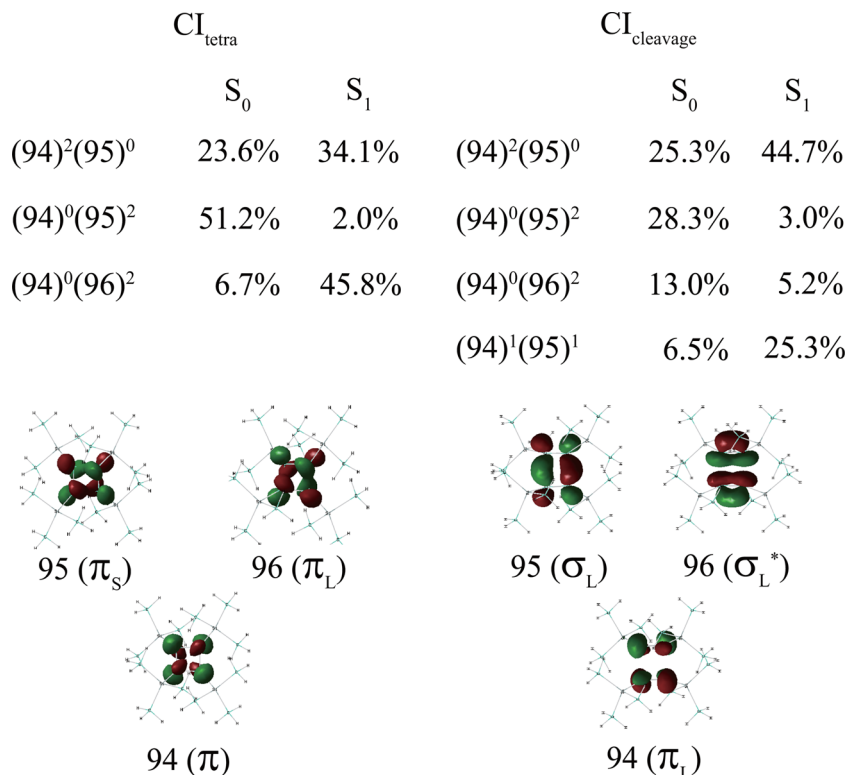


**Figure 6.** Illustration of natural orbitals 94–96, and the contributions of major components in  $S_1$  and  $S_0$  wavefunctions at  $\text{CI}_{\text{tetra}}$  and  $\text{CI}_{\text{cleavage}}$ .

**$S_1/S_0$  Conical Intersections.** On the  $S_1$  PES, two different  $S_1/S_0$  CI points are found and presented in Figure 5. Following the previous study of tetra-*tert*-butyl CBD (TB-CBD), we label one of them as  $\text{CI}_{\text{tetra}}^{26}$ , with an energy of 2.6 eV above  $S_0$  minimum of TMS-CBD, is connected to the TMS-THD minimum point on the  $S_0$  PES, accordingly, its geometry could be regarded as an interpolation between CBD and THD. Roughly speaking, it deviates from the minimum point of the  $S_1$  by lifting the atoms at two opposite corners away from the original CBD plane. At  $\text{CI}_{\text{tetra}}$ , the out-of-plane distortion leads to the hybridization of 2s and 2p atomic orbitals, which reduces the antibonding character in the original highest antibonding  $\pi$  orbital, and causes its energy to be lower than  $\pi_S$  and  $\pi_L$ . In this considerably stabilized orbital (labeled 94 in Figure 6), the four hybridized carbon atom orbitals located at four corners of the ring are weakly overlapped.

As shown in Figure 6, the adiabatic wave functions of  $S_1$  and  $S_0$  states share the same major component of  $(94)^2(95)^0$  at  $\text{CI}_{\text{tetra}}$  point. Besides,  $S_1$  has a predominant component of  $(94)^0(96)^2$ , whereas  $S_0$  is characterized as  $(94)^0(95)^2$ . Due to near-equalization of the four C–C bonds in the CBD ring, orbitals 95 and 96 are nearly degenerate, which could also diminish the energy difference between  $(94)^0(95)^2$  and  $(94)^0(96)^2$  configurations, leading to the mutual approaching of  $S_0$  and  $S_1$  potential energy surfaces at  $\text{CI}_{\text{tetra}}$  point. The derivative coupling vector and gradient difference vector at  $\text{CI}_{\text{tetra}}$  are illustrated in Figure 5. Linear combination of the two vectors could generate a pyramidalization mode connecting to THD framework.

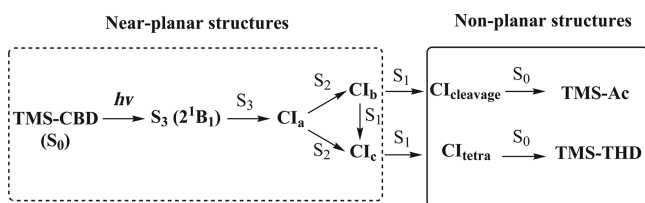
The other CI point, which is labeled  $\text{CI}_{\text{cleavage}}$  with an energy of 4.2 eV above  $S_0$  minimum of TMS-CBD, is connected to the dissociation products. Compared with  $\text{CI}_b$ , the longer C–C bonds are further stretched to 2.05 Å, the skeleton of the CBD ring is also distorted from the planar conformation as shown in Figure 5. Such geometrical change from  $\text{CI}_b$  to  $\text{CI}_{\text{cleavage}}$

significantly weakens the atomic orbital overlap along the longer C–C bonds. As a result, the two  $\sigma$  type orbitals 95 and 96 with, respectively, considerable bonding and antibonding characters along the longer C–C bonds, present clearly nonbonding characters at the  $\text{CI}_{\text{cleavage}}$  point and significantly take part in constructing both  $S_1$  and  $S_0$  wave functions. Orbital 94 ( $\pi_L$ ) is the other most active orbital in the two states, which shows strong antibonding character on the shorter C–C bonds and weak bonding character on the longer ones.

As shown in Figure 6, at  $\text{CI}_{\text{cleavage}}$ , the adiabatic wave functions of both  $S_1$  and  $S_0$  states share the same major component of  $(94)^2(95)^0$ . Besides this common configuration,  $S_1$  state has another major component of  $(94)^1(95)^1$ , which is inherited from the wave function at  $\text{CI}_b$ ; however  $(94)^0(95)^2$  configuration is the other major component in  $S_0$  state, and this configuration is the predominant component in the ground state wave function of TMS-CBD at its equilibrium geometry. The derivative coupling vector and gradient difference vector at  $\text{CI}_{\text{cleavage}}$  are illustrated in Figure 5. Combination of these two vectors could generate various vibrational modes, along one of which the TMS-CBD will dissociate into two TMS-Ac molecules.

After a detailed investigation of the critical points on relevant potential energy surfaces, a schematic diagram of the reaction mechanism is shown in Scheme 3. The photochemical processes of TMS-CBD isomerization and dissociation could be initiated from the FC excitation to the  $S_3$  state. The total relaxation paths could be divided into two stages in terms of geometrical changes of the CBD skeleton. In the first stage, following a series of state transitions as well as geometrical relaxations from  $S_3$  to  $S_1$ , the CBD skeleton approximately maintains its near-planar conformation. The second stage fulfills internal conversions from  $S_1$  to  $S_0$  via two nonplanar CI points,  $\text{CI}_{\text{cleavage}}$  and  $\text{CI}_{\text{tetra}}$ , respectively. In summary, two relaxation channels leading to

**Scheme 3. Schematic Diagram of the Photoreaction Paths for TMS-CBD through  $\sigma-\pi^*$  Single Excitation<sup>a</sup>**



<sup>a</sup>The solid and dash arrows indicate the relaxation channels leading to TMS-Ac and TMS-THD, respectively.

the dissociation product (TMS-CBD) and the isomerization product (TMS-Ac), respectively, are described in Scheme 3.

We note that a static characterization of critical points on the potential energy surfaces could only supply the electronic coupling vectors at MECIs, whereas the efficiency of a radiationless internal conversion process is also dependent on the vector of nuclear momentum.<sup>55</sup> This point is particularly important for  $S_1/S_0$  conversion process, where the vibronic relaxation could be a competitive process against the internal conversion discussed here, and this could be clarified by further nonadiabatic dynamics simulations.

## CONCLUSION

The mechanism of the photochemical reaction in TMS-CBD has been investigated using the CASSCF method. The vertical excitation energies of several low-lying excited states are computed and compared using CASSCF, MRMP, and EOM-CCSD methods. Our calculations suggest that the Franck-Condon excitation most probably corresponds to the excitation to the second  $^1B_1$  state ( $S_3$ ), which is attributed to the  $\sigma \rightarrow \pi$  single excitation, with an excitation energy available from low pressure mercury lamp irradiation.

The state transitions as well as geometrical relaxations in the excited states are discussed in detail by analyzing the minimum points as well as the conical intersections on relevant potential energy surfaces. Complete reaction channels have been suggested for the two major products, TMS-THD and TMS-Ac, which were reported experimentally. The first channel, which corresponds to the isomerization of the CBD skeleton to THD structure, is characterized by contracting the longer C–C bonds and via a tetra form conical intersection on  $S_2$  PES. The other channel is attributed to the CBD skeleton dissociation, producing two TMS-Ac molecules. This dissociation channel takes place by further stretching of the longer C–C bonds after excitation into  $S_3$  state, which makes it more competitive than the isomerization channel. These two possible relaxation paths can elucidate the mechanism of photochemical reactions of TMS-CBD upon irradiation of >300 nm.

Many CBD derivatives have been synthesized in the past decades, TMS-CBD is one of which showing unexpected thermodynamical stability at high temperatures, as well as fascinating photochemical behaviors. Thorough understanding of their physical and chemical properties requires careful treatment of the electronic effects of the substituent on chemical bonding in the CBD skeleton, with the dynamical electron correlations appropriately taken into consideration.

## ASSOCIATED CONTENT

### Supporting Information

Details of the computational results, including absolute energies, electronic wave functions, as well as Cartesian coordinates of optimized structures have been collected in the Supporting Information. This material is available free of charge via the Internet at <http://pubs.acs.org/>.

## AUTHOR INFORMATION

### Corresponding Author

\*E-mail: cgliu@nju.edu.cn. Phone: +86 (25) 83596756. Fax: +86 (25) 83596131.

### Notes

The authors declare no competing financial interest.

## ACKNOWLEDGMENTS

C.G.L. is grateful to Dr. Yihan Shao for the discussions on the theoretical methods involved in our work, as well as his generous help in correcting the language errors in the manuscript. This work is supported by China NSF (Grant Nos. 20873058, 21173116, 21473088), National Basic Research Program (Grant No. 2011CB808501). Part of the computational work was finished on our Inspur TS10000 cluster, and IBM HS22 blade-centers at the High Performance Computing Center of Nanjing University.

## REFERENCES

- (1) Emerson, G.; Watts, L.; Pettit, R. Cyclobutadiene- and benzocyclobutadiene- iron tricarbonyl complexes. *J. Am. Chem. Soc.* **1965**, *87*, 131–133.
- (2) Bally, T.; Masamune, S. Cyclobutadiene. *Tetrahedron* **1980**, *36*, 343–370.
- (3) Cram, D.; Tanner, M.; Thomas, R. The taming of cyclobutadiene. *Angew. Chem., Int. Ed. Engl.* **1991**, *30*, 1024–1027.
- (4) Balková, A.; Bartlett, R. J. A multireference coupled-cluster study of the ground state and lowest excited states of cyclobutadiene. *J. Chem. Phys.* **1994**, *101*, 8972–8987.
- (5) Deniz, A. A.; Peters, K. S.; Snyder, G. J. Experimental determination of the antiaromaticity of cyclobutadiene. *Science* **1999**, *286*, 1119–1122.
- (6) Moran, D.; Manoharan, M.; Heine, T.; Schleyer, P. v. R.  $\sigma$ -Antiaromaticity in cyclobutane, cubane, and other molecules with saturated four-membered Rings. *Org. Lett.* **2003**, *5*, 23–26.
- (7) Fattahi, A.; Lis, L.; Tian, Z.; Kass, S. R. The heat of formation of cyclobutadiene. *Angew. Chem., Int. Ed.* **2006**, *45*, 4984–4988.
- (8) Bally, T. Cyclobutadiene: The antiaromatic paradigm? *Angew. Chem., Int. Ed.* **2006**, *45*, 6616–6619.
- (9) Karadakov, P. B. Aromaticity and antiaromaticity in the low-lying electronic states of cyclooctatetraene. *J. Phys. Chem. A* **2008**, *112*, 12707–12713.
- (10) Wu, J. I.-C.; Mo, Y.; Evangelista, F. A.; Schleyer, P. v. R. Is cyclobutadiene really highly destabilized by antiaromaticity? *Chem. Commun.* **2012**, *48*, 8437–8439.
- (11) Maier, G. Tetrahedrane and cyclobutadiene. *Angew. Chem., Int. Ed. Engl.* **1988**, *27*, 309–332.
- (12) Schleyer, P. v. R. Introduction: aromaticity. *Chem. Rev.* **2001**, *101*, 1115–1118.
- (13) Schleyer, P. v. R. Introduction: delocalization-Pi and Sigma. *Chem. Rev.* **2005**, *105*, 3433–3435.
- (14) Masamune, S.; Ona, H.; Suda, M.; Leichter, L. Cyclobutadiene. *J. Chem. Soc. Chem. Commun.* **1972**, *23*, 1268–1269.
- (15) Sekiguchi, A.; Matsuo, T.; Watanabe, H. Synthesis and characterization of a cyclobutadiene dianion dilithium salt: Evidence for aromaticity. *J. Am. Chem. Soc.* **2000**, *122*, 5652–5653.

- (16) Ishii, K.; Kobayashi, N.; Matsuo, T.; Tanaka, M.; Sekiguchi, A. Observation of the predicted negative faraday a MCD term in a cyclobutadiene dianion. *J. Am. Chem. Soc.* **2001**, *123*, 5356–5357.
- (17) Maier, G.; Neudert, J.; Wolf, O. Tetrakis(trimethylsilyl)-cyclobutadiene and tetrakis (trimethylsilyl)tetrahedrane. *Angew. Chem., Int. Ed.* **2001**, *40*, 1674–1675.
- (18) Maier, G.; Neudert, J.; Wolf, O.; Pappusch, D.; Sekiguchi, A.; Tanaka, M.; Matsuo, T. Tetrakis(trimethylsilyl)tetrahedrane. *J. Am. Chem. Soc.* **2002**, *124*, 13819–13826.
- (19) Inagaki, Y.; Nakamoto, M.; Sekiguchi, A. Photoisomerization of perfluoroaryl tetrahedranes to perfluoroaryl cyclobutadienes. *J. Am. Chem. Soc.* **2011**, *133*, 16436–16439.
- (20) Maier, G.; Pfriem, S.; Schäfer, U.; Matusch, R. Tetra-tert-butyltetrahedrane. *Angew. Chem., Int. Ed. Engl.* **1978**, *17*, 520–521.
- (21) Maier, G.; Born, D. Tri-tert-butyl(trimethylsilyl)tricyclo[1.1.0.0<sup>2,4</sup>]butane a second tetrahedrane derivative. *Angew. Chem., Int. Ed. Engl.* **1989**, *28*, 1050–1052.
- (22) Kollmar, H. An MO theoretical study on the stability of tetrahedrane. *J. Am. Chem. Soc.* **1980**, *102*, 2617–2621.
- (23) Kollmar, H.; Carrion, F.; Dewar, M. J. S.; Bingham, R. C. Ground states of molecules. 58. The  $C_4H_4$  potential surface. *J. Am. Chem. Soc.* **1981**, *103*, 5292–5303.
- (24) Sumita, M.; Saito, K. Ground state potential energy surface between cyclobutadiene and tetrahedrane looked down from  $S_1/S_0$  conical intersections. *Tetrahedron* **2010**, *66*, 5212–5217.
- (25) Sumita, M.; Saito, K. Tetra-radical and ionic  $S_1/S_0$  conical intersections of cyclobutadiene. *Chem. Phys.* **2010**, *371*, 30–35.
- (26) Sumita, M.; Saito, K.; Tateyama, Y. Computational study on photo- and thermo-reactions between tetra-tert-butyl-substituted cyclobutadiene and tetrahedrane. *Comput. Theor. Chem.* **2011**, *969*, 44–52.
- (27) Nemirowski, A.; Reisenauer, H. P.; Schreiner, P. R. Tetrahedrane-dossier of an unknown. *Chem.—Eur. J.* **2006**, *12*, 7411–7420.
- (28) Arnold, B.; Michl, J. Ultraviolet and polarized infrared-spectroscopy of matrix-isolated cyclobutadiene and its isotopomers. *J. Phys. Chem.* **1993**, *97*, 13348–13354.
- (29) Knowles, P. J.; Werner, H. J. An efficient second-order MCSCF method for long configuration expansions. *Chem. Phys. Lett.* **1985**, *115*, 259–267.
- (30) Werner, H. J.; Knowles, P. J. A second order multiconfiguration SCF procedure with optimum convergence. *J. Chem. Phys.* **1985**, *82*, 5053–5063.
- (31) Bearpark, M. J.; Robb, M. A.; Schlegel, H. B. A direct method for the location of the lowest energy point on a potential surface crossing. *Chem. Phys. Lett.* **1994**, *223*, 269–274.
- (32) Korona, T.; Werner, H. J. Local treatment of electron excitations in the EOM-CCSD method. *J. Chem. Phys.* **2003**, *118*, 3006–3019.
- (33) Nakano, H. Quasidegenerate perturbation theory with multi-configurational self-consistent-field reference functions. *J. Chem. Phys.* **1993**, *99*, 7983–7992.
- (34) Wittek, H. A.; Choe, Y. K.; Finley, J. P.; Hirao, K. Intruder state avoidance multireference Moller-Plesset perturbation theory. *J. Comput. Chem.* **2002**, *23*, 957–965.
- (35) Levchenko, S.; Krylov, A. Equation-of-motion spin-flip coupled-cluster model with single and double substitutions: Theory and application to cyclobutadiene. *J. Chem. Phys.* **2004**, *120*, 175–185.
- (36) Hehre, W. J.; Ditchfield, R.; Pople, J. A. Self-consistent molecular-orbital methods 0.12. further extensions of gaussian-type basis sets for use in molecular-orbital studies of organic-molecules. *J. Chem. Phys.* **1972**, *56*, 2257–2261.
- (37) Hariharan, P. C.; Pople, J. A. Influence of polarization functions on molecular-orbital hydrogenation energies. *Theor. Chem. Acc.* **1973**, *28*, 213–222.
- (38) Hariharan, P. C.; Pople, J. A. Accuracy of AH<sub>n</sub> equilibrium geometries by single determinant molecular-orbital theory. *Mol. Phys.* **1974**, *27*, 209–214.
- (39) Gordon, M. S. The isomers of silacyclopropane. *Chem. Phys. Lett.* **1980**, *76*, 163–168.
- (40) Franci, M. M.; Pietro, W. J.; Hehre, W. J.; Binkley, J. S.; Gordon, M. S.; DeFrees, D. J.; Pople, J. A. Self-consistent molecular-orbital methods 0.23. A polarization-type basis set for second-row elements. *J. Chem. Phys.* **1982**, *77*, 3654–3665.
- (41) Hehre, W. J.; Stewart, R. F.; Pople, J. A. Self-consistent molecular-orbital methods.I. use of gaussian expansions of Slater-type atomic orbitals. *J. Chem. Phys.* **1969**, *51*, 2657–2664.
- (42) Collins, J. B.; von R. Schleyer, P.; Binkley, J. S.; Pople, J. A. Self-consistent molecular orbital methods. XVII. Geometries and binding energies of second-row molecules. A comparison of three basis sets. *J. Chem. Phys.* **1976**, *64*, 5142–5151.
- (43) Becke, A. D. Density-functional exchange-energy approximation with correct asymptotic-behavior. *Phys. Rev. A* **1988**, *38*, 3098–3100.
- (44) Lee, C. T.; Yang, W. T.; Parr, R. G. Development of the Colle-Salvetti correlation-energy formula into a functional of the electron-density. *Phys. Rev. B* **1988**, *37*, 785–789.
- (45) Becke, A. D. Density-functional Thermochemistry 0.3. the Role of exact exchange. *J. Chem. Phys.* **1993**, *98*, 5648–5652.
- (46) Stephens, P. J.; Devlin, F. J.; Chabalowski, C. F.; Frisch, M. J. Ab initio calculation of vibrational absorption and circular dichroism spectra using density functional force fields. *J. Phys. Chem.* **1994**, *98*, 11623–11627.
- (47) Frisch, M. J.; Trucks, G. W.; Schlegel, H. B.; Scuseria, G. E.; Robb, M. A.; Cheeseman, J. R.; Scalmani, G.; Barone, V.; Mennucci, B.; Petersson, G. A. et al. *Gaussian 09*, revision B.01, Gaussian, Inc.: Wallingford CT, 2010.
- (48) Werner, H.-J.; Knowles, P. J.; Lindh, R.; Manby, F. R.; Schütz, M.; Celani, P.; Korona, T.; Rauhut, G.; Amos, R. D.; Bernhardsson, A. et al. *MOLPRO*, version 2010.1, a package of ab initio programs, see <http://www.molpro.net>.
- (49) Schmidt, M. W.; Baldridge, K. K.; Boatz, J. A.; Elbert, S. T.; Gordon, M. S.; Jensen, J. H.; Koseki, S.; Matsunaga, N.; Nguyen, K. A.; Su, S.; Windus, T. L.; Dupuis, M.; Montgomery, J. A. General atomic and molecular electronic structure system. *J. Comput. Chem.* **1993**, *14*, 1347–1363.
- (50) Gordon, M. S.; Schmidt, M. W. In *Theory and Applications of Computational Chemistry*; Dykstra, C. E., Frenking, G., Kim, K. S., Scuseria, G. E., Eds.; Elsevier: Amsterdam, 2005; pp 1167–1189.
- (51) Eckert-Maksić, M.; Vazdar, M.; Barbatti, M.; Lischka, H.; Maksić, Z. B. Automerization reaction of cyclobutadiene and its barrier height: An ab initio benchmark multireference average-quadratic coupled cluster study. *J. Chem. Phys.* **2006**, *125*, 064310.
- (52) Nakamura, K.; Osamura, Y.; Iwata, S. Second-order Jahn-Teller effect of cyclobutadiene in low-lying states. An MCSCF study. *Chem. Phys.* **1989**, *136*, 67–77.
- (53) Sancho-García, J. C.; Pittner, J.; Čársky, P.; Hubač, I. Multireference coupled-cluster calculations on the energy of activation in the automerization of cyclobutadiene: Assessment of the state-specific multireference Brillouin-Wigner theory. *J. Chem. Phys.* **2000**, *112*, 8785–8788.
- (54) Borden, W. T.; Davidson, E. R. Theoretical studies of diradicals containing four  $\pi$  electrons. *Acc. Chem. Res.* **1981**, *14*, 69–76.
- (55) Tully, J. C. Molecular-dynamics with electronic-transitions. *J. Chem. Phys.* **1990**, *93*, 1061–1071.
- (56) Celani, P.; Robb, M. R.; Garavelli, M.; Bemardi, F.; Olivucci, M. Geometry optimization on a hypersphere. Application to finding reaction paths from a conical intersection. *Chem. Phys. Lett.* **1995**, *243*, 1–8.
- (57) Woywod, C.; Domcke, W.; Sobolewski, A.; Werner, H. Characterization of the  $S_1$ - $S_2$  conical intersection in pyrazine using ab initio multiconfiguration self-consistent-field and multireference configuration-interaction methods. *J. Chem. Phys.* **1994**, *100*, 1400–1413.
- (58) Kühl, A.; Domcke, W. Multilevel Redfield description of the dissipative dynamics at conical intersections. *J. Chem. Phys.* **2002**, *116*, 263–274.